Title

Near- and Extended-Edge X-Ray-Absorption Fine-Structure Spectroscopy Using Ultrafast Coherent High-Order Harmonic Supercontinua

Journal

Physical Review Letters, 120(9)

ISSN

0031-9007

Authors

Popmintchev, Dimitar
Galloway, Benjamin R
Chen, Ming-Chang
et al.

Publication Date

2018-03-02

DOI

10.1103/physrevlett.120.093002

Peer reviewed

Featured in Physics

Near- and Extended-Edge X-Ray-Absorption Fine-Structure Spectroscopy Using Ultrafast Coherent High-Order Harmonic Supercontinua

Dimitar Popmintchev,[1,*] Benjamin R. Galloway,[1] Ming-Chang Chen,[2] Franklin Dollar,[1] Christopher A. Mancuso,[1] Amelia Hankla,[1] Luis Miaja-Avila,[3] Galen O'Neil,[3] Justin M. Shaw,[3] Guangyu Fan,[4] Skirmantas Ališauskas,[4,5] Giedrius Andriukaitis,[4] Tadas Balčiunas,[4] Oliver D. Mücke,[6,7] Audrius Pugzlys,[4] Andrius Baltuška,[4] Henry C. Kapteyn,[1] Tenio Popmintchev,[1,†] and Margaret M. Murnane[1,‡]

[1]*JILA, University of Colorado at Boulder, Boulder, Colorado 80309-0440, USA*
[2]*National Tsing Hua University, Institute of Photonics Technologies, Hsinchu 30013, Taiwan*
[3]*National Institute of Standards and Technology, Boulder, Colorado 80305, USA*
[4]*Photonics Institute, TU Wien, Gusshausstrasse 27-387, A-1040 Vienna, Austria*
[5]*Deutsches Elektronen-Synchrotron DESY, Notkestraße 85, D-22607 Hamburg, Germany*
[6]*Center for Free Electron Laser Science (CFEL), Deutsches Elektronen-Synchrotron DESY, Notkestraße 85, D-22607 Hamburg, Germany*
[7]*The Hamburg Centre for Ultrafast Imaging, Luruper Chaussee 149, 22761 Hamburg, Germany*

(Received 24 July 2017; revised manuscript received 10 December 2017; published 1 March 2018)

Recent advances in high-order harmonic generation have made it possible to use a tabletop-scale setup to produce spatially and temporally coherent beams of light with bandwidth spanning 12 octaves, from the ultraviolet up to x-ray photon energies >1.6 keV. Here we demonstrate the use of this light for x-ray-absorption spectroscopy at the *K*- and *L*-absorption edges of solids at photon energies near 1 keV. We also report x-ray-absorption spectroscopy in the water window spectral region (284–543 eV) using a high flux high-order harmonic generation x-ray supercontinuum with 10^9 photons/s in 1% bandwidth, 3 orders of magnitude larger than has previously been possible using tabletop sources. Since this x-ray radiation emerges as a single attosecond-to-femtosecond pulse with peak brightness exceeding 10^{26} photons/s/mrad^2/mm^2/1% bandwidth, these novel coherent x-ray sources are ideal for probing the fastest molecular and materials processes on femtosecond-to-attosecond time scales and picometer length scales.

DOI: 10.1103/PhysRevLett.120.093002

Coherent x-ray spectroscopies are powerful probes of matter, bringing unique advantages that are complementary to visible or infrared spectroscopies. Techniques such as x-ray-absorption spectroscopy (XAS) can encode the instantaneous charge and spin state in the x-ray-absorption edge structure, giving additional information about the local structure, chemical nature, and electronic structure, as well as orbital and spin ordering phenomena. In particular, the extreme ultraviolet (EUV) to soft x-ray photon energy range from ~40 eV to above 1 keV is particularly relevant for probing bulk materials and interfaces. Examples include oxide materials (through the oxygen *K*-shell edge at 0.54 keV) or magnetic and superconducting materials (employing spectroscopies at the *M* and *L* edges). Angle-resolved photoemission spectroscopy can capture the dynamic electronic band structure, while XAS is sensitive to the electronic, spin, and geometric structure of molecules and materials. The near-edge x-ray-absorption fine structure (NEXAFS) originates from core level transitions to unoccupied states, while the oscillatory structure in the broadband x-ray absorption, called extended x-ray-absorption fine structure (EXAFS), results from modulations in the absorption probability caused by photoelectron interferences, which can be used to unambiguously determine the local atomic structure (within 10–20 Å) with picometer resolution using sources with nanometer scale wavelength. Essentially, these techniques provide a label-free, atomic-site-specific spectroscopy technique, since different elements have different characteristic core absorption edges in the soft x-ray region, and their exact positions depend on the local charge environment. Moreover, soft x rays can penetrate thick or opaque samples.

In comparison with x-ray crystallography, x-ray-absorption fine structure (XAFS) employs significantly lower x-ray photon energies, requires a broad or tunable spectrum, probes local atomic distribution, and does not need a crystalline sample. Indeed, XAFS is applicable to various phases of matter (i.e., crystals, gases, low concentration solutions, disordered solids, etc.), making it particularly well suited for probing dynamic processes that generally result in some level of disorder. XAFS can thus provide extensive chemical and structural information about the types of atoms present, their coordination numbers (number of neighboring atoms at particular

distances), mean interatomic distances, and disorder (using EXAFS), oxidation state, and coordination chemistry (using NEXAFS).

Past implementations of XAFS used both laser plasma emission and synchrotron radiation from large facilities (synchrotrons, Omega, NIF) and also from smaller laser-plasma-based facilities [1–4]. These incoherent soft x-ray sources typically provide a peak brightness of less than 10^{26} photons/s/mrad^2/mm^2/1% bandwidth with time resolution ~1 ps [5].

More recently, high-order harmonic generation (HHG) [6–12] sources have made it possible to implement coherent x-ray spectroscopies using a tabletop-scale apparatus [13–17]. These sources have unprecedented spatial and temporal coherence and are capable of extending the XAFS technique for measuring dynamics at attosecond-to-femtosecond time scales as well as providing picometer spatial resolution, with elemental and chemical specificity. In the EUV region of the spectrum at photon energies <100 eV, where bright HHG sources have been used for more than a decade, a broad range of applications in nano- and materials science have been demonstrated, including the investigations of how nanoscale energy flow differs from bulk [18,19], how fast a material can change its electronic or magnetic state [20–22], how fast spin currents control and enhance magnetization in materials [23,24], and more recently, how the band structure of a material influences photoemission [25]. In the latter case, recent work directly observed the fastest excited-state dynamics to date, measuring an excited-state lifetime of ~212 ± 30 as, for an electron excited ~20 eV above the Fermi level into a resonant transient state, as well as distinguishing attosecond charge scattering and screening in a material [26]. Many of these advances already have made use of the broadband nature of the HHG emission to access dynamics at multiple atomic sites simultaneously—essentially acting as a low-photon energy version of NEXAFS. These results already emphasize that these new sources can uniquely access new regimes for materials, and identify and control quantum processes at the nanoscale.

EXAFS requires absorption data over a broad spectral bandwidth >100 eV, which has only recently become possible [7–12] via HHG sources. When midinfrared (mid-IR) femtosecond lasers are used to drive HHG, ultrabroad coherent supercontinua are produced, with >1.3 keV tail-to-tail spectral width, spanning many characteristic x-ray edges (Fig. 1). Furthermore, mid-IR laser-driven HHG exhibits a time-gated phase matching that allows for optimized up-conversion while naturally confining the emission to a single isolated attosecond burst [9,27], and resulting in true supercontinua. The first pioneering works on EXAFS spectroscopy using tabletop HHG sources used a photon flux of 10^4 photons/s at 1 keV and 10^2 photons/s at 2 keV. Using these sources, static XAFS spectra were acquired at various absorption edges,

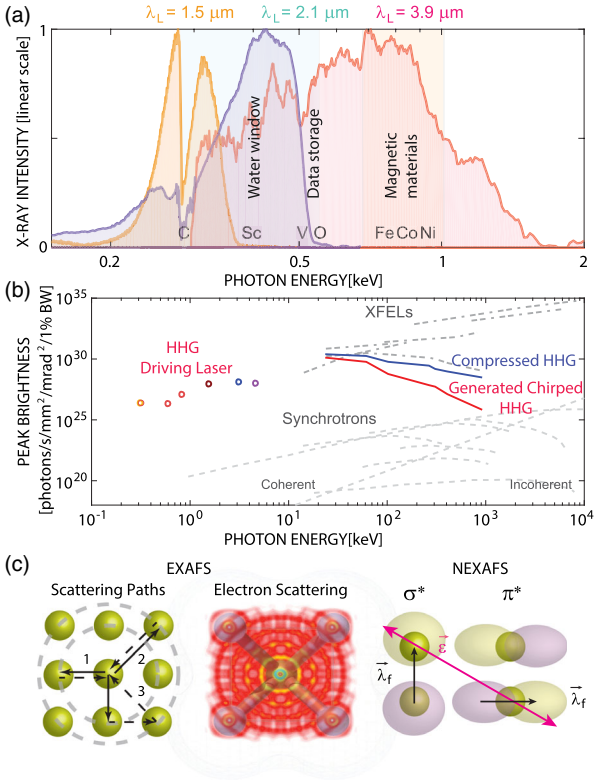

FIG. 1. (a) Three broadband soft x-ray supercontinua up to 0.36, 0.55, and 1.6 keV photon energies are generated using mid-IR driving lasers at 1.5, 2.1, and 3.9 μm, respectively, in He gas. (b) Peak brightness of coherent high-order harmonic x-ray sources (solid lines) using UV, visible, and IR driving lasers (circles). X-ray FELs (BESSY FEL, FLASH, LCLS, European XFEL, etc.) and synchrotron sources (BESSY II, Petra, etc.) are in dashed lines (BW-bandwidth) [32–35] (c) Left: Illustration showing the scattering paths of photoelectrons from the first (path 1) and second shell (path 2), as well as secondary rescattering (path 3). Center: Photoelectron scattering and interference of the electron-wave packet for a 2D planar lattice. Right: XAFS sensitivity to the polarization $\vec{\varepsilon}$ and final $\vec{\lambda}_f$ orbital direction.

and a dynamic edge shift with sub-ps resolution was observed in the XAFS spectra [28,29]. However, the low signal-to-noise ratio (SNR) and long acquisition times in such experiments lead to relatively large uncertainties. As a result, in the past, the large SNR that is required for XAFS measurements meant that large facilities were the only sources suitable for this type of spectroscopy [30,31].

With the development of femtosecond laser sources in the mid-IR, and their application to drive HHG in an optimized, phase-matched configuration, static NEXAFS at the sulfur and carbon edges were demonstrated [13], at the sulfur edge (~163 eV) employing a photon flux of ~10^9 photons/s, and at the carbon (C) edge (~282 eV) with a flux of 10^7 photons/s in 1% bandwidth [14,15,36].

Here we use bright, tabletop, broadband HHG supercontinua for NEXAFS and EXAFS spectroscopies at the K- and L-absorption edges to study the structure and chemistry

of solids. Specifically, we demonstrate the first XAFS spectroscopy at the K- and L-absorption edges of solids in the near-keV range using a high-order harmonic source. We also demonstrate x-ray-absorption spectroscopy in the water window spectral region (284–541 eV) using an x-ray supercontinuum with high flux 10^9 photons/s in 1% bandwidth, which is 3 orders of magnitude larger than fluxes previously demonstrated [10,36]. In the future, because this x-ray radiation emerges as a single isolated attosecond-to-femtosecond burst, with peak brightness exceeding 10^{26} photons/s/mrad^2/mm^2/1% bandwidth, these novel coherent x-ray sources will be ideal for dynamic probing of the fastest processes in molecules and materials on femtosecond-to-attosecond time and picometer length scales.

Two different mid-IR laser systems were used in this work. First, a 14 mJ, optical parametric chirped-pulse amplifier (OPCPA) at a wavelength of 3.9 μm with repetition rate of 20 Hz, and 80 fs pulse duration, producing a HHG supercontinuum spanning the EUV and the soft x-ray spectral region up to 1.6 keV (about 7.7 Å) with $\sim 2 \times 10^6$ photons/s in 1% bandwidth near ~1 keV. Further details of the OPCPA experimental beam line can be found in Ref. [12,37]. Second, an optical parametric amplifier (OPA) pumped by a 19.5 mJ, 20 fs, 1 kHz repetition rate Ti:sapphire laser. To avoid any nonlinearity from pulse propagation in air and to maintain excellent beam quality, the 20 fs Ti:sapphire pulses are stretched in the time domain to >150 fs FWHM and then recompressed to 20 fs using chirped mirrors placed just before each amplification stage of the OPA. This results in excellent beam quality profiles and short few-cycle pulse durations for the mid-IR light. We note that the driving lasers at 2.1 and 3.9 μm are derived from the idler beam of a parametric process and are passively carrier-envelope phase stable.

The OPA was used to produce a 2.75 mJ idler pulse with duration as short as ~26 fs or four optical cycles at 2.1 μm and a signal pulse with 4.5 mJ and a ~24 fs, five-cycle pulse duration when centered at 1.5 μm. The driving pulses were focused into a 1–5 cm long waveguide, with inner diameter of 150–400 μm, and filled with ~10–20 atm of helium gas. The generated HHG supercontinuum extends up to photon energies of 550 and 360 eV for the idler and signal beams, respectively [Fig. 1(a)]. The high photon flux of $>10^9$ photons/s in 1% bandwidth in the water window spectral region is more than 1000 times larger than previously demonstrated [10,36]. The estimated HHG flux after the waveguide is summarized in Fig. 1(b). These bright ultrabroadband HHG pulses with laserlike properties allow us to obtain high-quality EXAFS data, from which picometer-resolution structural information is extracted by accumulating only a small number of laser shots. Moreover, our data show excellent agreement with theory. In our experimental apparatus, the HHG generation setup is followed by an x-ray spectrometer with a spectral resolution of $\lambda/\Delta\lambda > 1000$ (EUV to soft x-ray region), followed by thin metal filters to separate the fundamental from the HHG supercontinuum and the samples. The spectral data are then captured on an x-ray charged coupled device (CCD) camera. By inserting and removing the samples, the spectrally resolved absorptivity can be determined with high accuracy and analyzed with the software programs ATHENA and ARTEMIS [38]. The spectrometer wavelength scale is calibrated using multiple characteristic absorption features and edges of thin film filters.

EXAFS is a universal response of matter interacting with x-ray light near an absorption edge. This quantum phenomenon can be understood in a simple three-step model, where an incident x-ray photon is absorbed by an atom, which leads to the ejection of a photoelectron from a core shell. Then the photoelectron is scattered from neighboring nonexcited atoms, and the quantum interferences of the outgoing and incoming scattered electron waves lead to an energy-dependent variation of the x-ray-absorption probability [Fig. 1(c)]. In addition, these modulations are enriched by secondary and higher-order rescatterings that are also imprinted in the absorption or fluorescence spectra.

For long EUV–x-ray pulses, the maximum distance that can be probed through XAFS is limited by the mean free path of the electron (10–20 Å). For shorter HHG pulses (<10 as) this distance could be expected to be reduced as electron scattering events are time delayed.

Figure 2(b) shows the experimentally extracted EXAFS function at the L-absorption edges (~700 eV) of a monoatomic body-centered-cubic (bcc) Fe thin foil at room temperature, both in k space and in real space.

These data were taken using a HHG supercontinuum source spanning from EUV to 1.6 keV, and the data are analyzed using the ATHENA and ARTEMIS software [38]. A straightforward method for obtaining spatial distributions correlated to the interatomic distances is to take a Fourier transform of the k-scaled EXAFS function [Figs. 2(b) and 2(c)]. Fitting the first peak of spatial data to theory, we extract a nearest first shell distance of 2.48 ± 0.03 Å (eightfold degenerate) and second shell distance of 2.87 ± 0.03 Å (sixfold degenerate), the latter value also being the lattice constant for a bcc crystal structure. Independent x-ray diffraction measurements affirm a bcc structure with a lattice constant of 286.68 ± 0.03 pm for this sample. Peaks from multiple rescattering paths can be difficult to distinguish in general, and we use continuous Cauchy wavelet transform to decompose the EXAFS amplitude terms in real and reciprocal space [Fig. 2(a)] [39]. Such a 2D plot can provide information for the k and R range of each nearest neighbor shell contribution and discriminate the shell distances for complex systems [Fig. 2(c)].

The HHG supercontinuum driven by $\lambda = 2.1$ μm pulses does not extend to as high photon energies compared to the 4 μm laser; however, they are well suited for soft x-ray spectroscopy of importance for chemical and biological studies (water window region), as well as for investigation

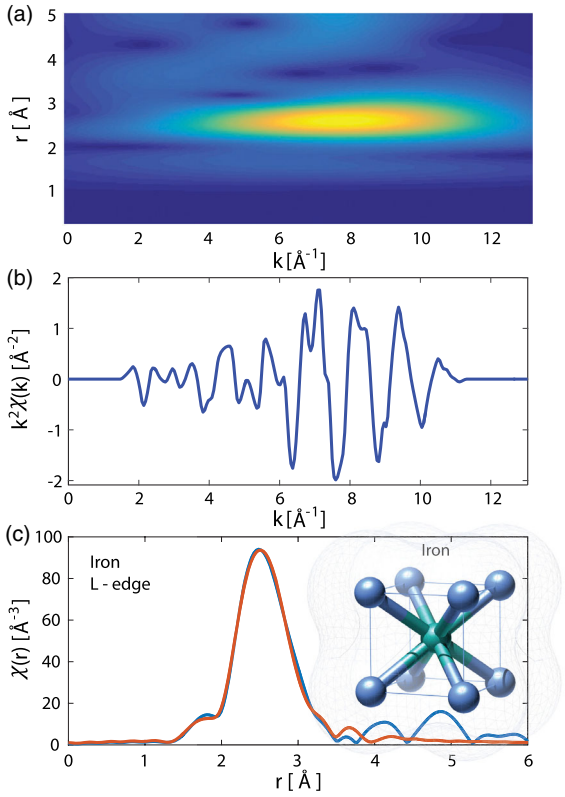

FIG. 2. Experimental XAFS spectroscopy of a Fe thin film using 4 μm-driven HHG supercontinuum up to 1.6 keV. (a) Continuous Cauchy wavelet transform analysis (modulus) near the Fe L edge (0.7 keV), (b) k^2-scaled EXAFS function in k space extending to 12 Å^{-1}. (c) Experimental real-space EXAFS function (blue), uncorrected for δ phase shifts, with first peak fitted (red) to theory. Inset shows a Fe bcc unit cell.

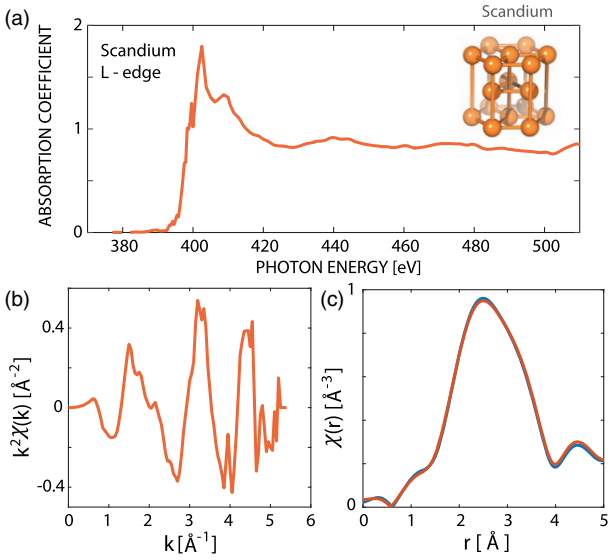

FIG. 3. Experimental XAFS spectroscopy near the Sc L edge, using a 2 μm-driven HHG supercontinuum up to 550 eV. (a) The normalized absorption coefficient of Sc near the L-absorption edge at 398 eV. (b) k^2-scaled EXAFS function in k space extending to >5 Å^{-1}. (c) Experimental R-space EXAFS function (blue), not corrected for δ phase shifts, and fitted (red) to theory. The real-space EXAFS function exhibits a broad peak. Inset shows a Sc hcp unit cell.

of phase transitions in inorganic materials such as VO_2, of interest for fast optical modulators and data storage devices. Here, extracting structural information from the EXAFS data leads to larger uncertainties since the k range, over which the data are recorded, is limited to below 5–6 Å^{-1}. Nevertheless, these spectra are well suited for NEXAFS spectroscopies without the need of wavelength scanning. Figure 3 shows the absorption coefficient and the R- and k-space EXAFS function distributions for a monoatomic Sc thin foil at the L-absorption edge (~398 eV). Our data are in excellent agreement with the CXRO database [40]. Fitting the spatial distribution data [Fig. 3(c)], we obtain a nearest first shell distance of 3.25 ± 0.05 Å (sixfold degenerate) and the second shell distance of 3.30 ± 0.05 Å (sixfold degenerate), in good agreement with the expected interatomic length.

Coherent x-ray spectroscopies have an important additional advantage of being able to uncover the excited-state dynamics with elemental specificity, i.e., oxidation state, magnetic state, or charge localization to specific elements, giving information about the electronic structures (i.e., valence, bands, and charge), as well as orbital and spin ordering phenomena. The spectral features near an absorption edge are dictated by the atomic orbital overlap and the valence of the atoms. Modulations in the absorption spectra within 50 eV of an edge are labeled as near-edge x-ray-absorption fine structure. This x-ray bandwidth requirement is readily achieved by mid-IR-driven HHG supercontinua, and the optimal driving laser wavelength can be chosen for a phase-matched HHG cutoff energy moderately higher than the absorption edge energy [10,12,41]. For experiments near the chemically relevant carbon K edge at 284.2 eV, this prescribes a driving laser wavelength of $\lambda \sim 1.3$–1.6 μm. Tuning the signal beam from a mid-IR OPA to 1.5 μm, the HHG x-ray supercontinuum is centered near ~300 eV, with a bandwidth of >180 eV. Figure 4 compares the near-edge absorption structures of mylar and parylene at the carbon K-absorption edge. These data show that we can resolve energy shifts as small as 0.2 eV in the $1s$-π^* and $1s$-σ^* absorption peaks, due to the sensitivity to the different molecular functional groups. The resolution in these measurements is close to 0.2 eV or $\lambda/\Delta\lambda \sim 1400$. Each spectrum was recorded for 0.05 s (50 laser shots), averaged over 30 exposures; in principle, these XAFS could be obtained in a single-shot mode. We identify transitions from $1s$ (K shell) to the antibonding π^* orbital ($1s$ to π^*) of unsaturated C=C bonds of the aromatic ring near 285 eV [42]. The large peak at 285 eV shows predominantly unsaturated C bonds (i.e., sp^2 hybridization). The peak around ~289 eV is generally considered to be a mixed state of $1s$ to the antibonding σ^* orbital and $1s$-$3p$ (Rydberg-like) orbitals of the aromatic ring structure [Fig. 4(b)] [42].

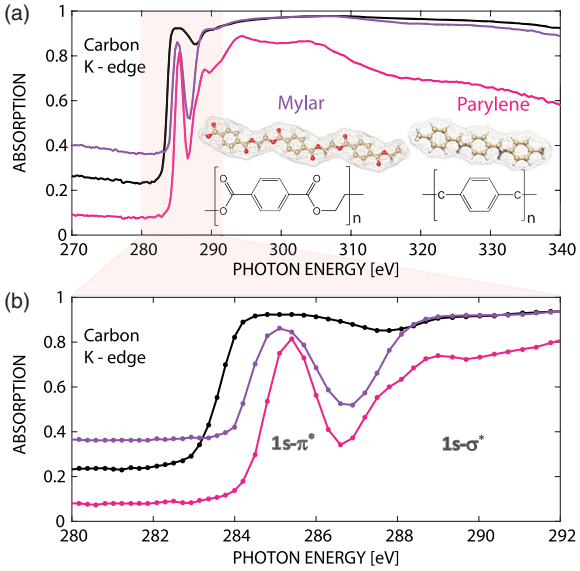

FIG. 4. Experimental NEXAFS spectroscopy near the carbon K edge using a 1.5 μm-driven HHG supercontinuum up to 360 eV. (a) NEXAFS of C-containing polymers [mylar (violet) and parylene (pink)], at the carbon K edge. Also plotted is the experimental absorption spectrum of a carbon thin film (black) for reference. Inset: Molecular structure of mylar and parylene rendered for trimers (C atoms in brown, O in red, H in white). (b) Close-up view showing peaks due to transitions from $1s$ to both π^* and σ^* orbitals.

NEXAFS taken with polarized x-ray light is also sensitive to molecular orientation. For the $1s$ spherically symmetric initial state and polarized final state, the transition intensity is proportional to the $\cos^2(\vartheta_{\vec{\varepsilon},\vec{\lambda}_f})$, where $\vartheta_{\vec{\varepsilon},\vec{\lambda}_f}$ is the angle between the polarization of the electric field ($\vec{\varepsilon}$) and the direction ($\vec{\lambda}_f$) of the final orbital [Fig. 1(c)], and is maximized when the polarization is parallel to $\vec{\lambda}_f$. In our experiment, $\vec{\varepsilon}$ lies in the plane of the sample.

In summary, using coherent high-order harmonic broadband x-ray supercontinua generated by mid-IR lasers, we demonstrate first extended-edge absorption spectroscopy (coherent EXAFS) at the K and L edges of elements at near-keV photon energies using a tabletop-scale apparatus. We also demonstrate near-edge soft x-ray-absorption spectroscopy in the water window spectral region (coherent NEXAFS).

Finally, the unique temporal coherence of the HHG source—since the HHG emission in these spectral regions is in the form of a single subfemtosecond chirped burst—opens the path for capturing coupled charge, spin, and structural dynamics with femtosecond-to-attosecond time resolution and picometer spatial resolution. With some prior knowledge, these techniques can provide extensive spatiotemporal and chemical imaging information $(4+1)$D of the local atomic structure of materials, including (1) the types of atoms that are present, coordination numbers (number of neighboring atoms at particular distances), interatomic distances, as well as disorder (using EXAFS), and (2) the oxidation state and coordination chemistry (i.e., symmetries, isomerism, etc.) (using NEXAFS) [35]. For more information see the Supplemental Material [43].

M. M. M. and H. C. K. acknowledge support from the Department of Energy BES Award No. DE-FG02-99ER14982 (experiment) as well as a MURI grant from the Air Force Office of Scientific Research under Award No. FA9550-16-1-0121 (theory). B. R. G. gratefully acknowledges support from the National Nuclear Security Administration Stewardship Science Graduate Fellowship program. C. A. M. acknowledges support from the National Science Foundation Graduate Research Fellowship under Grant No. DGE 1144083.

*Dimitar.Popmintchev@gmail.com
†Present address: Physics Department, University of California San Diego, La Jolla, California 92093, USA. Tenio.Popmintchev@physics.ucsd.edu
‡Margaret.Murnane@colorado.edu

[1] M. H. Key and R. J. Hutcheon, Spectroscopy of laser-produced plasmas, Adv. At. Mol. Phys. **16**, 201 (1980).
[2] H. C. Gerritsen, H. van Brug, M. Beerlage, and M. J. Van der Wiel, A polychromator for (S)EXAFS using a laser generated plasma as soft X-ray source, Nucl. Instrum. Methods Phys. Res., Sect. A **238**, 546 (1985).
[3] D. E. Sayers, E. A. Stern, and F. W. Lytle, New Technique for Investigating Noncrystalline Structures: Fourier Analysis of the Extended X-Ray–Absorption Fine Structure, Phys. Rev. Lett. **27**, 1204 (1971).
[4] L. Miaja-Avila *et al.*, Ultrafast Time-Resolved Hard X-Ray Emission Spectroscopy on a Tabletop, Phys. Rev. X **6**, 031047 (2016).
[5] I. Robinson, G. Gruebel, and S. Mochrie, Focus on X-ray beams with high coherence, New J. Phys. **12**, 035002 (2010).
[6] A. Rundquist, C. G. Durfee, Z. Chang, C. Herne, S. Backus, M. M. Murnane, and H. C. Kapteyn, Phase-matched generation of coherent soft X-rays, Science **280**, 1412 (1998).
[7] E. J. Takahashi, T. Kanai, K. L. Ishikawa, Y. Nabekawa, and K. Midorikawa, Coherent Water Window X Ray by Phase-Matched High-Order Harmonic Generation in Neutral Media, Phys. Rev. Lett. **101**, 253901 (2008).
[8] T. Popmintchev, M.-C. Chen, O. Cohen, M. E. Grisham, J. J. Rocca, M. M. Murnane, and H. C. Kapteyn, Extended phase matching of high harmonics driven by mid-infrared light, Opt. Lett. **33**, 2128 (2008).
[9] T. Popmintchev, M.-C. Chen, A. Bahabad, M. Gerrity, P. Sidorenko, O. Cohen, I. P. Christov, M. M. Murnane, and H. C. Kapteyn, Phase matching of high harmonic generation in the soft and hard X-ray regions of the spectrum, Proc. Natl. Acad. Sci. U.S.A. **106**, 10516 (2009).
[10] M.-C. Chen, P. Arpin, T. Popmintchev, M. Gerrity, B. Zhang, M. Seaberg, D. Popmintchev, M. M. Murnane, and H. C. Kapteyn, Bright, Coherent, Ultrafast Soft X-Ray Harmonics Spanning the Water Window from a Tabletop Light Source, Phys. Rev. Lett. **105**, 173901 (2010).

[11] T. Popmintchev, M.-C. Chen, P. Arpin, M. M. Murnane, and H. C. Kapteyn, The attosecond nonlinear optics of bright coherent X-ray generation, Nat. Photonics **4**, 822 (2010).
[12] T. Popmintchev *et al.*, Bright Coherent Ultrahigh Harmonics in the keV X-ray Regime from Mid-Infrared Femtosecond Lasers, Science **336**, 1287 (2012).
[13] C. Ding, W. Xiong, T. Fan, D. D. Hickstein, T. Popmintchev, X. Zhang, M. Walls, M. M. Murnane, and H. C. Kapteyn, High flux coherent super-continuum soft X-ray source driven by a single-stage, 10mJ, Ti:sapphire amplifier-pumped OPA, Opt. Express **22**, 6194 (2014).
[14] K. Kaneshima, N. Ishii, T. Kanai, S. Watanabe, and J. Itatani, Laser-Based Soft X-Ray Light Source Resolving X-ray Absorption Near Edge Structure at the Carbon K Edge, in *Proceedings of CLEO 2015* (Optical Society of America, San Jose, CA, 2015), p. JTh5C.2.
[15] S. L. Cousin, F. Silva, S. Teichmann, M. Hemmer, B. Buades, and J. Biegert, High-flux table-top soft x-ray source driven by sub-2-cycle, CEP stable, 1.85-μm 1 -kHz pulses for carbon K-edge spectroscopy, Opt. Lett. **39**, 5383 (2014).
[16] Y. Pertot *et al.*, Time-resolved x-ray absorption spectroscopy with a water window high-harmonic source, Science **355**, 264 (2017).
[17] A. R. Attar, A. Bhattacherjee, C. D. Pemmaraju, K. Schnorr, K. D. Closser, D. Prendergast, and S. R. Leone, Femtosecond x-ray spectroscopy of an electrocyclic ring-opening reaction, Science **356**, 54 (2017).
[18] M. E. Siemens, Q. Li, R. Yang, K. A. Nelson, E. H. Anderson, M. M. Murnane, and H. C. Kapteyn, Quasi-ballistic thermal transport from nanoscale interfaces observed using ultrafast coherent soft X-ray beams, Nat. Mater. **9**, 26 (2010).
[19] K. M. Hoogeboom-Pot *et al.*, A new regime of nanoscale thermal transport: Collective diffusion increases dissipation efficiency, Proc. Natl. Acad. Sci. U.S.A. **112**, 4846 (2015).
[20] S. Mathias *et al.*, Probing the timescale of the exchange interaction in a ferromagnetic alloy, Proc. Natl. Acad. Sci. U.S.A. **109**, 4792 (2012).
[21] C. La-O-Vorakiat *et al.*, Ultrafast Demagnetization Measurements Using Extreme Ultraviolet Light: Comparison of Electronic and Magnetic Contributions, Phys. Rev. X **2**, 011005 (2012).
[22] C. La-O-Vorakiat *et al.*, Ultrafast Demagnetization Dynamics at the M Edges of Magnetic Elements Observed Using a Tabletop High-Harmonic Soft X-Ray Source, Phys. Rev. Lett. **103**, 257402 (2009).
[23] D. Rudolf *et al.*, Ultrafast magnetization enhancement in metallic multilayers driven by superdiffusive spin current, Nat. Commun. **3**, 1037 (2012).
[24] E. Turgut *et al.*, Controlling the Competition between Optically Induced Ultrafast Spin-Flip Scattering and Spin Transport in Magnetic Multilayers, Phys. Rev. Lett. **110**, 197201 (2013).
[25] Z. Tao, C. Chen, T. Szilvási, M. Keller, M. Mavrikakis, H. Kapteyn, and M. Murnane, Direct time-domain observation of attosecond final-state lifetimes in photoemission from solids, Science **353**, 62 (2016).
[26] C. Chen, Z. Tao, A. Carr, P. Matyba, T. Szilvási, S. Emmerich, M. Piecuch, M. Keller, D. Zusin, S. Eich, M. Rollinger, W. You, S. Mathias, U. Thumm, M. Mavrikakis, M. Aeschlimann, P. M. Oppeneer, H. Kapteyn, and M. Murnane, Distinguishing attosecond electron–electron scattering and screening in transition metals, Proc. Natl. Acad. Sci. U.S.A. **114**, E5300 (2017).
[27] M.-C. Chen *et al.*, Generation of bright isolated attosecond soft X-ray pulses driven by multicycle midinfrared lasers, Proc. Natl. Acad. Sci. U.S.A. **111**, E2361 (2014).
[28] E. Seres, J. Seres, and C. Spielmann, X-ray absorption spectroscopy in the keV range with laser generated high harmonic radiation, Appl. Phys. Lett. **89**, 181919 (2006).
[29] E. Seres, J. Seres, and C. Spielmann, Time resolved spectroscopy with femtosecond soft-x-ray pulses, Appl. Phys. A **96**, 43 (2009).
[30] P. A. Lee, P. H. Citrin, P. Eisenberger, and B. M. Kincaid, Extended x-ray absorption fine structure–its strengths and limitations as a structural tool, Rev. Mod. Phys. **53**, 769 (1981).
[31] G. Bunker, Sources of Noise in EXAFS Experiments, http://gbxafs.iit.edu/training/Noise.pdf.
[32] European XFEL, http://www.xfel.eu/.
[33] National Research Council, *Controlling the Quantum World: The Science of Atoms, Molecules, and Photons* (National Academies Press, Washington, DC, 2007), Vol. 2.
[34] SLAC, https://heds.slac.stanford.edu/our-research/record-peak-brightness.
[35] D. Popmintchev, Ph.D. thesis, University of Colorado at Boulder, 2016 (ASIN: B01N9G9JVZ).
[36] S. Teichmann, F. Silva, S. L. Cousin, M. Hemmer, and J. Biegert, 0.5-keV Soft X-ray attosecond continua, Nat. Commun. **7**, 11493 (2016).
[37] G. Andriukaitis, T. Balciunas, S. Alisauskas, A. Pugzlys, A. Baltuska, T. Popmintchev, M.-C. Chen, M. M. Murnane, and H. C. Kapteyn, 90 GW peak power few-cycle mid-infrared pulses from an optical parametric amplifier, Opt. Lett. **36**, 2755 (2011).
[38] B. Ravel and M. Newville, ATHENA, ARTEMIS, HEPHAESTUS: data analysis for X-ray absorption spectroscopy using IFEFFIT, J. Synchrotron Radiat. **12**, 537 (2005).
[39] M. Muñoz, F. Farges, and P. Argoul, Continuous Cauchy wavelet transform of XAFS spectra, Phys. Scr. **T115**, 221 (2005).
[40] http://henke.lbl.gov/.
[41] D. Popmintchev *et al.*, Ultraviolet surprise: Efficient soft x-ray high-harmonic generation in multiply ionized plasmas, Science **350**, 1225 (2015).
[42] Y. Ma, H. Yang, J. Guo, C. Sathe, A. Agui, and J. Nordgren, Structural and electronic properties of low dielectric constant fluorinated amorphous carbon films, Appl. Phys. Lett. **72**, 3353 (1998).
[43] See Supplemental Material athttp://link.aps.org/supplemental/10.1103/PhysRevLett.120.093002 for raw and analyzed data and methods used to estimate the HHG properties in the main text, which includes Refs. [44,45].
[44] Q. Shen, X-ray flux, brilliance and coherence of the proposed Cornell energy-recovery synchrotron source, CHESS Tech. Memo. 01-002, 2001.
[45] P. Shukla, J. Lawrence, and Y. Zhang, Understanding laser beam brightness: A review and new prospective in material processing, Opt. Laser Technol. **75**, 40 (2015).

Supplemental Materials for

Near- and Extended-Edge X-Ray-Absorption Fine-Structure Spectroscopy Using Ultrafast Coherent High-Order Harmonic Supercontinua

Dimitar Popmintchev[1]*, Benjamin R. Galloway[1], Ming-Chang Chen[2], Franklin Dollar[1], Christopher A. Mancuso[1], Amelia Hankla[1], Luis Miaja-Avila[3], Galen O'Neil[3], Justin M. Shaw[3], Guangyu Fan[4], Skirmantas Ališauskas[4,5], Giedrius Andriukaitis[4], Tadas Balčiunas[4], Oliver D. Mücke[6,7], Audrius Pugzlys[4], Andrius Baltuška[4], Henry C. Kapteyn[1], Tenio Popmintchev[1]*, Margaret M. Murnane[1]*

[1]*JILA, University of Colorado at Boulder, Boulder, CO 80309-0440 USA*

[2]*National Tsing Hua University, Institute of Photonics Technologies, Hsinchu 30013, Taiwan*

[3] *National Institute of Standards and Technology, Boulder, CO 80305, USA*

[4]*Photonics Institute, TU Wien, Gusshausstrasse 27-387, A-1040 Vienna, Austria*

[5]*Deutsches Elektronen-Synchrotron DESY, Notkestraße 85, D-22607 Hamburg, Germany*

[6]*Center for Free Electron Laser Science (CFEL), Deutsches Elektronen-Synchrotron DESY, Notkestraße 85, D-22607 Hamburg, Germany*

[7]*The Hamburg Centre for Ultrafast Imaging, Luruper Chaussee 149, 22761 Hamburg, Germany*

This PDF file includes:

- Supplemental Text
- Figures S1 to S3
- Tables S1 to S2
- References S1 to S7

In these Supplemental Materials, we provide raw and analyzed data used in the main text. We discuss methods used to estimate the HHG peak brightness and peak power of the HHG sources. In addition, we show independent raw data of X-ray Bragg scattering measurement of a thin Fe metal film.

Methods used for evaluation of the peak power and brightness:

We estimate the peak power of the generated X-ray pulses and the HHG driving lasers as: $P_{peak} = E/\tau$, where E is the energy per pulse of the source and τ is the pulse duration. The chromatic dispersion of the HHG pulses is discussed in the next section [1, 2], Figure S2.

We evaluate the peak brightness (brilliance) as the number of photons per pulse, per unit volume in a six dimensional phase space that includes both transverse and longitudinal directions [3]:

$$P_B = \frac{Energy}{\mathcal{V}_{phase}} = \frac{N_{ph} 2.3556^2}{(2\pi)^3 (\Delta E/E)\tau \underbrace{(\pi \mathcal{w}_0^2)}_{Area} \underbrace{\left(2\pi(1-\cos(\theta))\right)}_{\Omega_{solid}}} \quad (1)$$

, where θ is the half angle of divergence, $\mathcal{w}_0$ is the beam radius. The radiative throughput is proportional to the Lagrange invariant and can be written for small angles as: Area $\cdot\, \Omega_{solid} \cong \left(M_x^2 M_y^2\right)\lambda_L^2$, where M_x^2, M_y^2 are M squared values in x, and y transverse direction. The additional factor 2.355 arise from conversions from standard deviation to FWHM for ΔE, and τ. N_{ph} is the number of photons per pulse. The peak brightness increases with photon energy and scales as $P_{\mathrm{B}} \propto 1/\lambda^3$, for same number of photons. For other definitions, see [4]. The peak brightness for synchrotrons and XFELs is usually reported in 0.1% bandwidth (BW) and here it is scaled to 1% bandwidth for comparison with the HHG X-ray sources.

Driving IR laser	**1.5 µm**	**2.1 µm**	**3.9 µm**	**Typical synchrotron**	**European XFEL***
Repetition rate	1 kHz	1kHz	20 Hz	200 MHz	1-10MHz
Cutoff photon energy	360 eV	550 eV	1.6 keV	10 keV	10 keV
X-ray flux $\left[\frac{photons}{pulse\ 1\%BW}\right]$	$\sim 5\cdot10^6$	$\sim 10^6$	$\sim 10^5$	$\sim 10^7$	$\sim 10^{14}$
X-ray flux $\left[\frac{photons}{\mathrm{s}\ 1\%BW}\right]$	$\sim 5\cdot10^9$	$\sim 10^9$	$\sim 2\cdot10^6$	$\sim 10^{15}$	$\sim 10^{20}$
Peak brightness $\left[\frac{photons}{s\ mrad^2\ mm^2\ 1\%BW}\right]$	$\sim 8\cdot10^{27}$	$\sim 2\cdot10^{27}$	$\sim 6\cdot10^{25}$	$<10^{26}$	$\sim 5\cdot10^{34}$
X-ray pulse duration (transform-limited pulse duration)	~400 as (20 as)	~600 as (10 as)	~1.2 fs (2.5 as)	> ps 50 fs (slicing)	<100fs
Fractional bandwidth $\lambda/\Delta\lambda$	3	2	1	10	100
Source coherence	Spatial and temporal	Spatial and temporal	Spatial and temporal	Partial Spatial and temporal	Spatial (temporal**)

Table S1. Estimated flux and peak values of high harmonic soft X-ray supercontinua generated in He, used in this paper and typical values for synchrotron and XFEL sources. (*Theoretically projected values [5], ** Not implemented currently) HHG pulse durations are from [1, 2].

Evaluation of the pulse duration:

The X-ray pulse duration is estimated, from the chromatic dispersion acquired during the process of X-ray generation, for transform-limited driving laser pulses [2]. We evaluate the group delay dispersion (GDD) and higher orders, by taking the successive derivatives $D^{(n)} = -d^{n-1}t/d\omega_q^{n-1}(t)$, for each dispersion order n, where t represents the group delay of the classical electron. The Taylor expansion of

the harmonics phase: $\varphi_q(\omega) = \sum D^{(n)}(\omega - \omega_0)^n/n!$, is valid for slowly varying phase, which is extremely well justified here. The group delay dispersion and higher orders are given as:

$$D^{(n)} = \frac{\tau_L^{cycle}}{U_p^{n-1}} \kappa^{(n)}(E_q) \tag{2}$$

where $\kappa^n(E_q)$ are semianalytical, smooth functions that depend on the harmonic energy. The $\kappa^{(n)}/c$ coefficients as defined in Table S2 are evaluated numerically and plotted in Figure S1, where $\kappa^{(2)}/c = \alpha$, $\kappa^{(3)}/c = \beta$, $\kappa^{(4)}/c = \gamma$.

Figure S1 and Table S2 show the group delay dispersion and higher dispersion orders up to the fourth order. Higher order dispersions are progressively smaller and do not affect significantly the pulse shape.

Dispersion		**GDD [as^2]**	**TOD [as^3]**	**FOD [as^4]**
		$\alpha \frac{\lambda_L[\mu\text{m}]}{U_P[\text{keV}]}$	$\beta \frac{\lambda_L[\mu\text{m}]}{U_P^2[\text{keV}]}$	$\gamma \frac{\lambda_L[\mu\text{m}]}{U_P^3[\text{keV}]}$
Thumb rule	**short trajectory**	$\alpha \sim 150$	$\beta \sim -3$	$\gamma \sim 30$
	long trajectory	$\alpha \sim -130$	$\beta \sim 0.7$	$\gamma \sim -40$
Important for		$GDD > \tau_0^2$	$TOD > \tau_0^3$	$FOD > \tau_0^4$

Table S2 Semi-analytical expressions for the chirp and higher dispersion orders at phase-matching parameters for atom and ion species. α, β, γ coefficients are energy dependent and are plotted in Figure S1 for transform-limited driving laser pulse.

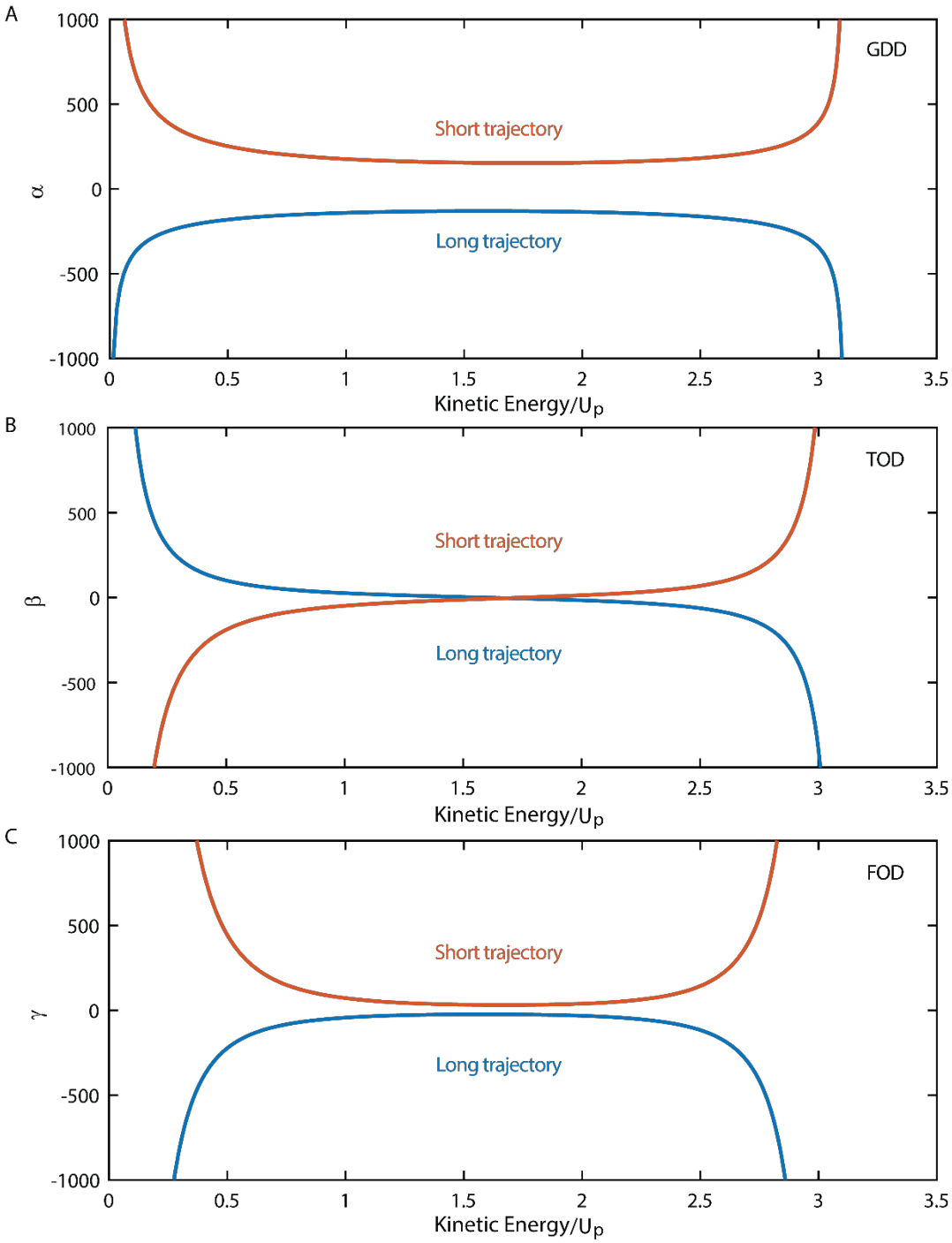

Figure S1 Coefficients α, β, γ (in units as defined in Table S2) for the short and long electron trajectory. **A)** group delay dispersion (GDD). The smooth curves have long energy range of almost equal GDD apart from the low and cutoff frequencies. **B)** Third order dispersion (TOD) **C**) Fourth order dispersion. TOD and FOD have negligible contributions compared to the GDD.

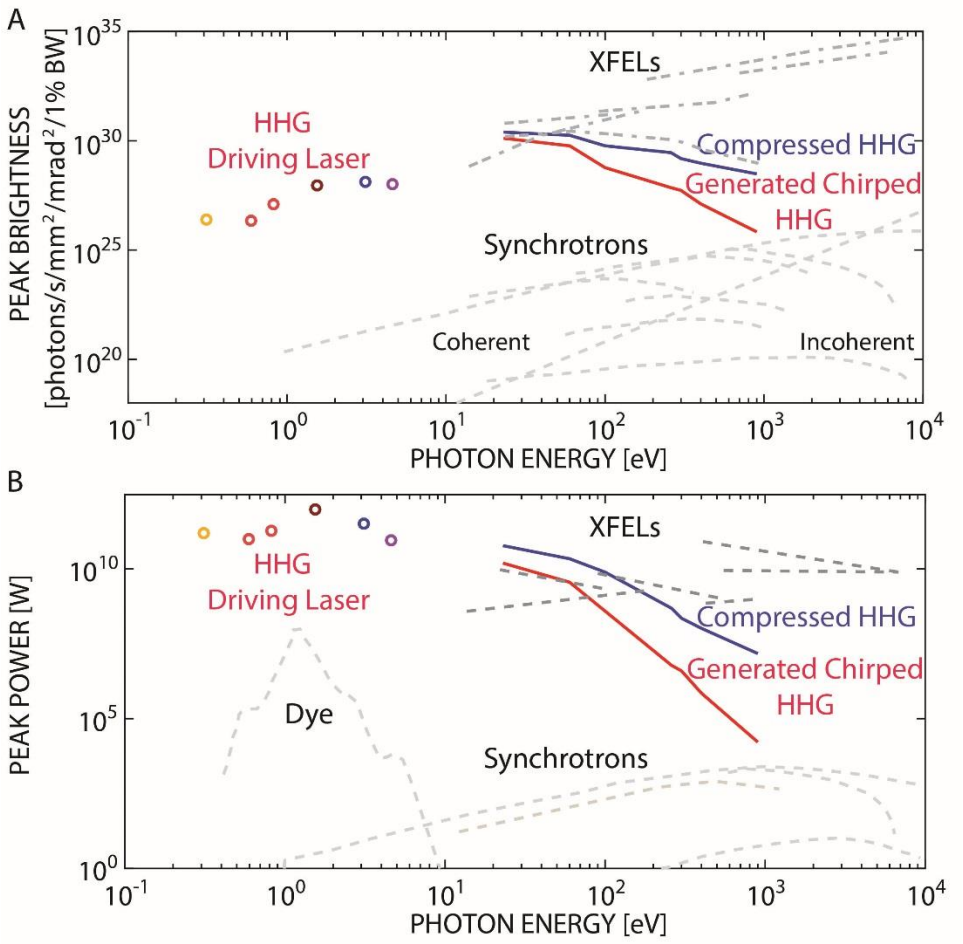

Figure S2. A) Peak brightness (brilliance) and **B)** Peak power of coherent high-harmonic X-ray sources using UV, visible and IR driving lasers (solid lines), compared to X-ray FELs and synchrotron sources (dashed lines). (Driving lasers used for HHG shown in circles - 3.9 μm , 2.1 μm , 1.5 μm , 0.8 μm , 0.4 μm , 0.27 μm). Data is compiled from various sources [2, 5-7].

X-ray absorption fine structure scattering

EXAFS is a universal response of matter interacting with X-ray light near an absorption edge. This quantum phenomenon can be understood in a simple three-step model, where an incident X-ray photon is absorbed by an atom, which leads to the ejection of a photoelectron from a core-shell. Then the photoelectron is scattered from neighboring non-excited atoms, and the quantum interferences of the outgoing and incoming scattered electron waves lead to an energy-dependent variation of the X-ray absorption probability (Figure 1B). In addition, these modulations are enriched by secondary and higher-order rescattering events that are also imprinted in the absorption or fluorescence spectra. In such picture, the absorption probability is modeled with an EXAFS function χ(k) :

$$\underbrace{\frac{\mu - \mu_o}{\mu_o}}_{experiment} = \chi(k) \cong \underbrace{\sum_i \frac{N_i A}{kR_i^2} sin(2kR_i + \delta_i)\, e^{\left(-\frac{2R_i}{k_i}\right)} e^{\left(-2k^2\sigma_i^2\right)}}_{theory} \quad (3)$$

, where μ is the total absorption coefficient and μ_o is the portion that corresponds to the slowly varying background of a single isolated atom absorption. Various electron scattering paths i (Figure 1B) contribute to different oscillation frequencies in the XAFS spectra. A is the backscattering amplitude, N_i is the number of scattering atoms in a particular shell, δ_i is the combined phase shift due to absorption and rescattering, κ_i is the electron mean free path, R_i is the half path length between the absorbing atom and the i coordination shell, σ_i is a disorder parameter and k is the electron wave number: $k[\text{Å}^{-1}] \approx 0.512\sqrt{(E - E_{edge})[eV]}$.

For EUV –x-ray pulses longer than 10 as, the maximum distance that can be probed through XAFS is limited by the mean free path of the electron (10 –20 Å). For shorter HHG pulses (<10 as) this distance could be expected to be significantly reduced. This limitation could arise from the fact that the HHG photon needs to be present at the absorbing atom during the electron scattering events in order to see a modulated absorption probability, and in general, photons travel faster than electrons.

X-ray diffraction characterization of Fe thin film

The X-ray Bragg diffraction was obtained using an X-ray tube with a water-cooled Cu anode to generate 8 keV, Cu $K\alpha$ radiation with a wavelength of ~0.15nm. All measurements were performed using parallel beam optics in a symmetric $\vartheta - 2\vartheta$ geometry. Figure S3 shows the X-ray diffraction spectrum of the Fe sample. Analysis of the data indicates a body-centered cubic (bcc) structure with a lattice constant of 286.68±0.03pm. This is within error of the tabulated value of 286.65pm for bcc Fe. The data is calibrated

using a polycrystalline silicon reference sample to correct for any offsets in the scattering angles. We observe no presence of oxide peaks or additional phases.

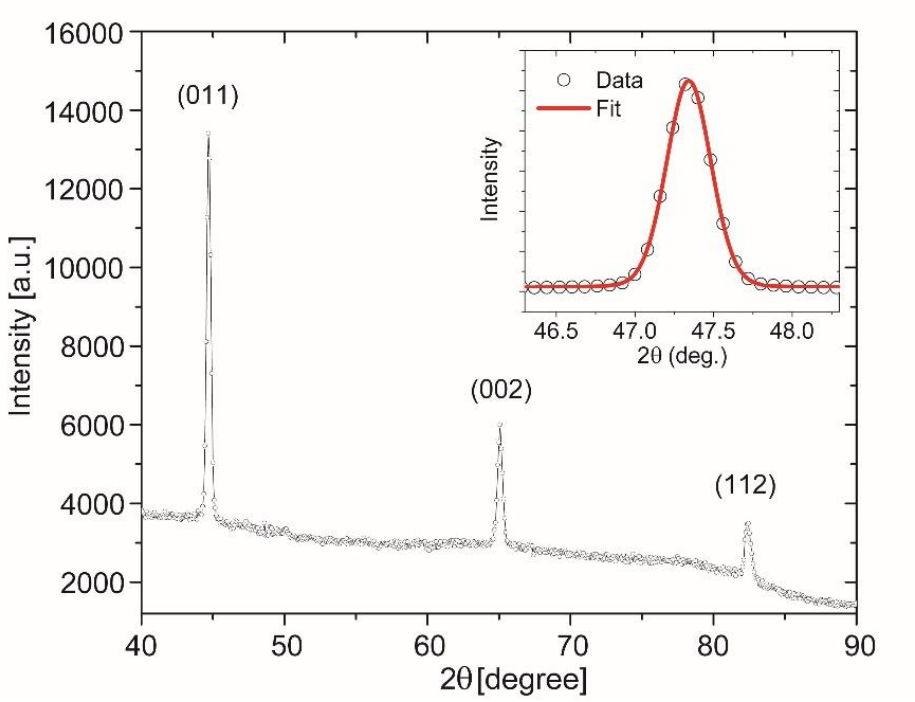

Figure S3. X-ray diffraction data, showing the first few diffraction peaks for Fe thin film. The data indicates a body-centered cubic structure (bcc) with a lattice constant of 286.68±0.03pm.

References

[1] D. Popmintchev et al., Science **350**, 1225 (2015).
[2] D. Popmintchev, Quantum and Extreme Nonlinear Optics Design of Coherent Ultrafast X-ray Light and Applications, Thesis (ASIN: B01N9G9JVZ), 2016.
[3] Q. Shen, X-ray flux, brilliance and coherence of the proposed Cornell energy-recovery synchrotron source, 2001.
[4] P. Shukla, J. Lawrence, and Y. Zhang, Optics & Laser Technology **75**, 40 (2015).
[5] European XFEL http://www.xfel.eu/.
[6] National Reasearch Council, Controlling the quantum world: the science of atoms, molecules, and photons (National Academies Press, 2007), Vol. 2.
[7] SLAC https://heds.slac.stanford.edu/our-research/record-peak-brightness.